Acta Materialia 153 (2018) 290–302

Contents lists available at ScienceDirect

Acta Materialia

journal homepage: www.elsevier.com/locate/actamat

Full length article

The effect of phase chemistry on the extent of strengthening mechanisms in model Ni-Cr-Al-Ti-Mo based superalloys

A.J. Goodfellow [a], E.I. Galindo-Nava [a], K.A. Christofidou [a], N.G. Jones [a], C.D. Boyer [b], T.L. Martin [c], P.A.J. Bagot [c], M.C. Hardy [d], H.J. Stone [a, *]

[a] Department of Materials Science and Metallurgy, University of Cambridge, 27 Charles Babbage Road, Cambridge, CB3 0FS, UK
[b] Canadian Neutron Beam Centre, Chalk River, Ontario, K0J 1J0, Canada
[c] Department of Materials, University of Oxford, Parks Road, Oxford, OX1 3PH, UK
[d] Rolls-Royce plc, PO Box 31, Derby, DE24 8BJ, UK

ARTICLE INFO

Article history:
Received 28 February 2018
Received in revised form
14 March 2018
Accepted 27 April 2018
Available online 3 May 2018

Keywords:
Superalloy
Mechanical properties
Modelling
Electron microscopy
Atom probe tomography

ABSTRACT

The exceptional mechanical properties of polycrystalline nickel-based superalloys arise through various concurrent strengthening mechanisms. Whilst these mechanisms are generally understood, consensus has yet to be established on the precise contribution of each to the overall alloy strength. Furthermore, changes in alloy chemistry influence several different mechanisms, making the assessment of individual alloying elements complex. In this study, a series of model quinary Ni-based superalloys has been investigated to systematically study the effect of varying Mo content on the contributing strengthening mechanisms. Using microstructural data, the yield strength was modelled by summing the individual effects of solid solution in both the γ and γ′ phases, coherency, grain boundary and precipitation strengthening. The total predicted yield stress increased with Mo content despite the diminishing contribution of precipitation strengthening. It is shown that solid solution strengthening of the ordered γ′ precipitate phase is a key contributor to the overall strength, and that variations in composition between the tertiary and secondary γ′ lead to significant changes in mechanical properties that should be accounted for in models of alloy strength.

1. Introduction

Polycrystalline nickel based superalloys are currently the material of choice for many components in gas turbine engines due to their superior high temperature strength and creep resistance. These valuable mechanical properties arise through the presence of coherent, ordered $L1_2$ (γ′) precipitates of multimodal size distributions embedded within a disordered A1 (γ) matrix phase [1]. Ni-based superalloys also benefit from a number of other concurrent strengthening mechanisms, including solid solution and grain boundary strengthening, in addition to those mechanisms inherent to precipitation strengthening itself.

A number of models exist to describe the individual strengthening mechanisms, including grain boundary strengthening, solid solution hardening of the γ phase and particle shear [2–7]. Whilst these studies effectively predicted the yield strength of the alloys under investigation, not all relevant effects have been universally incorporated into these models. For instance, Galindo-Nava et al. [8] predicted particle shear effects in superalloys with both monomodal and multimodal γ′ size distributions, although the phase chemistry was assumed to be constant, and neither solid solution strengthening in the γ′ nor coherency strengthening were considered. Kozar et al. [6] included solid solution strengthening in the γ′, but the effect of multimodal size distributions on particle shear was not accounted for. Similarly, whilst Ahmadi et al. [9] included the effects of coherency, grain boundary, solid solution and precipitate strengthening in predicting the yield strength of AllVac 718plus, the effect of variable γ′ phase composition, or particle size distribution were not incorporated into the models.

Previous studies using advanced characterisation techniques, such as high resolution scanning electron microscopy (HR-SEM), scanning transmission electron microscopy with energy-dispersive X-ray analysis (STEM-EDX) and atom probe tomography (APT), have identified that different γ′ size distributions display variations in chemical composition [10–12]. Such variations may be expected

* Corresponding author.
E-mail addresses: hwrdstn@gmail.com, hjs1002@cam.ac.uk (H.J. Stone).

https://doi.org/10.1016/j.actamat.2018.04.064

to significantly affect the mechanical properties, but these effects have not been quantified within existing physical models of superalloy strength. A unified model of the main strengthening mechanisms that takes into account variations in the size and composition of the phases is necessary if such predictions are to be effectively used to optimise the properties of superalloys, and to define processing routes that can deliver specific microstructures.

In this study, a series of model quinary, polycrystalline Ni-based superalloys with varying Mo content was investigated to assess the extent of individual strengthening mechanisms on the overall yield strength. The variation in Mo content was chosen to explore its role on the various strengthening mechanisms as it is a strong matrix solid solution hardener and affects the coherency strength via the lattice misfit. The alloys were studied using SEM, TEM and APT to fully characterise the particle size distributions and phase chemistries. This enabled the yield strength to be predicted with physically based models, using experimentally determined input values. Experimental measurements of the mechanical properties were obtained by compression testing and these results were compared to the model predictions. In addition to the overall yield strength, the individual effects of solid solution, precipitation, coherency and grain boundary strengthening were determined.

2. Experimental methods

The nominal compositions of the alloys studied are given in Table 1. The Mo content was systematically varied from 0 to 5 at. %, whilst the Al, Ti and Cr contents remained constant. Mo has a large atomic radius and is known to partition preferentially to the γ phase. As such, the composition of the γ' phase was anticipated to remain approximately constant across the series, which would allow the lattice misfit and γ solid solution strength to be changed without expected variations in the anti-phase boundary energy (APBE), thereby minimising the number of variables investigated.

Elements of 99.9% purity or higher were weighed out, vacuum induction melted (VIM) and poured into a steel mold to produce 10 mm diameter cylindrical bars. Differential Scanning Calorimetry (DSC) on the as-cast material was carried out on a NETZCH 404 instrument under flowing argon, using heating and cooling rates of 10 °C min^{-1} between room temperature and 1450 °C. From these data, a suitable temperature range for homogenisation in the single-phase γ region was identified for each alloy.

All samples were encapsulated in Ar-backfilled quartz ampoules and subsequently underwent the same homogenisation treatment at 1250 °C (above the γ' solvus temperature) for 22 h to reduce casting segregation and dissolve any primary γ'. This was followed by an aging treatment at 760 °C for 16 h. The alloys were air cooled following both homogenisation and ageing heat treatments. DSC of the aged alloys was carried out to determine the key transition temperatures of each alloy.

Scanning Electron Microscopy (SEM) was performed on an FEI Nova NanoSEM to determine the volume fraction of the secondary γ' precipitates in each alloy. Samples were polished to a 0.06 μm finish, and imaged in Backscattered Electron (BSE) mode at an operating voltage of ~5 keV. A quantitative value for the secondary γ' volume fraction was obtained via thresholding of the microstructural images acquired using ImageJ software [13]. SEM with Energy Dispersive X-ray spectroscopy (EDX) was carried out on 5 large areas of each sample, spaced across the full sample area, in order to determine the extent of compositional variations across the samples.

Table 1
Compositions (in at.%) of the model quinary alloys studied.

	Alloy 0	Alloy 1	Alloy 2	Alloy 3	Alloy 4	Alloy 5
Al (at.%)	6	6	6	6	6	6
Ti (at.%)	5	5	5	5	5	5
Cr (at.%)	15	15	15	15	15	15
Mo (at.%)	0	1	2	3	4	5
Ni (at.%)	Bal.	Bal.	Bal.	Bal.	Bal.	Bal.

Both electropolished samples and extraction replicas were prepared for imaging and compositional analysis using transmission electron microscopy (TEM). Electropolished samples were used for determining the composition of the γ matrix phase at the thin regions where no γ' precipitates were visible. However, the composition of the γ' phase could not be reliably determined by this method, since the visible γ' precipitates may have indiscernible regions of γ matrix above or below, which would be sampled by the electron beam, thereby affecting the deduced composition. Hence, extraction replicas of the γ' were utilized in order to obtain a more reliable measure of the composition of the γ' phase.

Electropolishing was carried out at −5 °C using a solution of 5% perchloric acid in methanol, a voltage of 20 V and a current of approximately 180 mA. Extraction replicas were obtained by electrolytically etching specimens polished to a 0.5 μm finish in a solution of 10% phosphoric acid in water at 3 V, until a blue halo appeared on the sample surface. To remove over etched particles, a few drops of formvar in chloroform solution were deposited on the surface of the sample to attach an acetate sheet. Once dry, the acetate was peeled off along with the over etched particles. Next, the samples were sputter coated with carbon and this carbon film was scored into ~2 mm squares. Finally, electrolytic etching was carried out in a solution of 20% perchloric acid in ethanol at 10 V until the carbon coating began to float off. The specimens were then removed into distilled water and the carbon films caught on copper TEM grids. Scanning Transmission Electron Microscopy (STEM) imaging and Energy Dispersive X-ray spectroscopy (EDX) were carried out at an accelerating voltage of 200 keV using an FEI Tecnai Osiris TEM equipped with an FEI Super-X EDX detector.

Further compositional analysis was performed by Atom Probe Tomography (APT) on a LEAP 5000 XR instrument, for two of the alloys with differing Mo contents (0 and 3 at.% Mo). Needle shaped specimens of 0.5 mm cross-section were produced by electro-discharge machining before electropolishing, first in a 10% perchloric acid in acetic acid solution at 22 V (DC), and subsequently in a 2% perchloric acid in 2-Butoxyethanol solution at 23 V. APT of the electropolished samples was then carried out in laser mode (wavelength of 355 nm), using a pulse energy of 50 pJ and a pulse rate of 200 kHz at a stage temperature of 50 K.

STEM images of the extraction replicas were used to determine the γ' particle size distributions (PSDs) of each alloy. A minimum of 300 secondary and 300 tertiary precipitates were traced manually to distinguish overlapping particles, and the equivalent circular diameters were obtained using the ImageJ software [13]. The individual precipitate sizes were binned to a histogram using the Freedman-Diaconis method [14], and fitted with a lognormal function (Equation (1)) using Igor Pro (WaveMetrics, Lake Oswego, OR, USA). The median (e^{μ_L}) was taken as the average precipitate size of each alloy, and the associated uncertainty was given as the width of the lognormal function from this median value ($e^{(\mu_L+\sigma_L)}$ and $e^{(\mu_L-\sigma_L)}$). w_L and σ_L are the standard deviations of the lognormal distribution and the coefficient μ_L obtained using Igor Pro, respectively.

$$f(x) = \frac{1}{x w_L \sqrt{2\pi}} e^{-\left[\frac{(\ln(x)-\mu_L)^2}{2w_L^2}\right]} \quad (1)$$

Neutron diffraction at room temperature was performed at the Canadian Neutron Beam Centre (CNBC) facility in Chalk River, Canada, on the C2 powder diffractometer. The wavelength of the incident beam was determined to be 1.33 Å through calibration using an Al_2O_3 standard. During diffraction data acquisition, the samples were rotated to minimize texture effects. For each sample, data were collected for 3 h at room temperature within a 2θ range of 36–116° using a position sensitive detector. To determine the lattice parameters of the γ and γ′ phases, the superlattice reflections were first individually fitted with Gaussian functions (Equation (2)) using Igor Pro.

$$f(x) = \frac{A}{w_G\sqrt{2\pi}}\, e^{-\left[\frac{(x-\mu_G)^2}{2w_G^2}\right]} \tag{2}$$

where w_G is the standard deviation, μ_G is the position constant of the Gaussian function, and A is the integral area. The associated γ′ lattice parameters ($a_{\gamma'}$) were subsequently found using the Nelson-Riley function [15], Equation (3).

$$(\delta a/a)_{abs} = \frac{1}{2}\left\{\frac{\cos^2\theta}{\sin^2\theta} + \frac{\cos^2\theta}{\theta}\right\} \tag{3}$$

The γ lattice parameters (a_γ) were found by fitting two Gaussian functions to each fundamental peak, one of which had its position constrained to that of the associated γ′ peak position, in line with previous studies on superalloys [16,17]. The Nelson-Riley function (Equation (3)) was again used to convert peak position to a value for lattice parameter. The experimental lattice misfit (δ) was subsequently determined using Equation (4).

$$\delta = \frac{2\left(a_{\gamma'} - a_\gamma\right)}{\left(a_{\gamma'} + a_\gamma\right)} \tag{4}$$

To experimentally determine the mechanical properties of the alloys, compression testing was carried out at room temperature using a low cycle fatigue machine comprising a 100 kN Mayes servohydraulic frame with an Instron 8800 controller. Both toe and compliance corrections were manually applied to the data. The associated uncertainty in the data was taken as the standard deviation of repeat measurements of each data point.

3. Modelling

3.1. Yield stress modelling

The superior strength of Ni-based superalloys stems from a number of different mechanisms, including; grain boundary (Hall-Petch) strengthening σ_{HP}, precipitate shear resistance σ_p, dislocation bypassing of the γ′ precipitates (Orowan stress) σ_{Oro}, solid solution hardening σ_{sss}, and coherency strengthening, σ_{coh}. The physical models used for each strengthening mechanism are briefly described in the following sections. These contributions are summed to give the overall yield strength σ_Y. Different methods of summation exist in the literature [2,18,19], but a superior fit to experimental data has been found using a linear summation [6,8], therefore Equation (5) has been used in the present study.

$$\sigma_Y = \sigma_{HP} + \sigma_p + \sigma_{sss} + \sigma_{Oro} + \sigma_{coh} \tag{5}$$

3.2. Grain boundary strengthening σ_{HP}

The extent of grain boundary strengthening is described by the Hall-Petch relation: $\sigma_{HP} = \frac{k_{HP}}{\sqrt{D}}$, where D is the grain size and k_{HP} is the Hall-Petch constant, which for superalloys has been determined to be 750 MPa $\mu m^{-1/2}$ [8].

3.3. Orowan stress σ_{Oro}

It has been shown in previous work that the contribution of the Orowan stress to the overall yield strength is very low in alloys with multimodal particle size distributions similar to those exhibited by the alloys considered in this study. Therefore, the Orowan contributions to strength were considered negligible in this study [8].

3.4. Precipitate shear and anti-phase boundary energy

The mechanisms of particle shear are well established. However, inconsistencies have arisen in the literature regarding how to unify both the weak and strong-pair dislocation coupling regimes. These configurations are found when precipitate size is smaller or larger than a critical radius r_m, respectively [20], as defined in Ref. [8]. In the present study, a unified model for the precipitate strength in both monomodal and multimodal γ′ size distributions has been utilized to overcome these issues [8].

For alloys with monomodal γ′ distributions, the critical shear stress required to cut a γ′ particle of size r is:

$$\tau_p = \frac{\gamma_{APB} l}{2b(\Lambda + 2r)} \tag{6}$$

where l is the length of the leading dislocation cutting through the particle, γ_{APB} the anti-phase boundary energy, b the magnitude of the Burgers vector and Λ is an effective distance between particles, of radius r, being sampled by a bowing (weak-pair coupling) or straight (strong-pair coupling) dislocation. In the weak-pair case ($r < r_m$), $l = 2r_m$, but in the strong-pair case ($r > r_m$), $l = 2\sqrt{r^2 - (r - r_m)^2}$. In the unified approach, $\Lambda = \max\left(\sqrt{\frac{\mu b^2}{2\gamma_{APB} r}}\sqrt{\frac{2\pi}{3f_{\gamma'}}}r,\ \sqrt{\frac{2\pi}{3f_{\gamma'}}}r - l\right)$, where $f_{\gamma'}$ is the total γ′ volume fraction.

Equation (6) was expanded to account for the effects of a bimodal precipitate size distribution. The contributions of the secondary and tertiary γ′ distributions to the total strength were weighted according to their relative particle number densities N_{sec} and N_{ter}, since the weak and strong pair-coupling models are based on dislocation interactions with individual precipitates. These number densities are defined as $N_{sec} = \frac{f_{sec}}{\pi r_{sec}^2}$ and $N_{ter} = \frac{f_{ter}}{\pi r_{ter}^2}$ respectively, where f_{sec} and r_{sec} are the volume fraction and average radius of the secondary γ′ precipitates, and f_{ter} and r_{ter} are those of the tertiary γ′. The shear stress τ_p required for dislocation motion, including secondary and tertiary γ′ effects is then calculated by:

$$\tau_p = \tau_{p,sec}\frac{N_{sec}}{N_{sec} + N_{ter}} + \tau_{p,ter}\frac{N_{ter}}{N_{sec} + N_{ter}} \tag{7}$$

Where $\tau_{p,sec}$ and $\tau_{p,ter}$ are the contributions of the secondary and tertiary γ′ precipitates respectively, and are computed with Equation (6).

It is clear from Equation (6) that the Anti-Phase Boundary Energy (APBE) associated with the ordered γ′ precipitate phase is one of the main parameters dictating alloy strength. The APBE depends on the composition of each precipitate, thus its value may be

expected to differ in the secondary and tertiary γ′ distributions if they have different compositions.

In the present study, the APBE was modelled by two methods to show that the effect of variations in chemical composition on particle shear are not method-specific; the CalPhaD-based (Calculation of Phase Diagrams) approach detailed by Crudden et al. [21] and by a simple linear mixtures approach based on density functional theory (DFT) calculations derived in the same work [21].

The phase compositions determined experimentally for both the secondary and tertiary γ′ phases were used to obtain a distinct value of the APBE in both distributions of γ′. It has been shown previously that the APT technique is much better suited to determination of the Al content in Ni-based superalloys than TEM as a result of the absorption of the low energy K emissions from this element [10]. Therefore, throughout this work, an average of the APT data was used to describe the Al content of these alloys, and this was assumed to be the same in each alloy studied. STEM EDX was used to determine the content of the remaining elements since this technique provides a convenient method for taking multiple repeat measurements, which was not possible with APT. Additionally, a very good correlation between APT and STEM EDX data has been shown previously, with the exception of Al for the reason provided above [10].

In the CalPhaD approach, an Ising model is employed to determine long-range ordering between nearest-neighbour interactions by relating interchange energies between the ordered (γ′) and disordered (γ) phases. ThermoCalc was used to determine the enthalpies of the disordered phase and an ordered phase of the same composition. These were converted to interaction energies for the first, second and third nearest neighbour atoms ($V^{(1)}$, $V^{(2)}$, $V^{(3)}$) by the method detailed by Crudden et al. [21], and the APBE was subsequently calculated using Equation (8), where a is the lattice parameter of the γ′ phase.

$$\gamma_{APB} = \frac{1}{\sqrt{3}a^2}\left(V^{(1)} + V^{(2)} + V^{(3)}\right) \tag{8}$$

The DFT approach also approximates the interchange energy by comparing the internal energy of supercells of ternary $Ni_3(Al,X)$ and A1 random solid solution, where X is the alloying element in the γ′. Crudden et al. [21] proposed a model for the APB energy in multicomponent Ni-based superalloys based on these results by extrapolating the values predicted between Ni-25 A l (at.%) and Ni-12.5Al-12.5X (at.%) with a linear fit according to the equation:

$$\gamma_{APB} = \gamma^0_{APB} + \sum_i k_i x_i^{\gamma'} \tag{9}$$

where γ^0_{APB} is the APBE of Ni_3Al and $x_i^{\gamma'}$ is the concentration of element i in the γ′. The coefficients k_i are constants specific to each element. The value for the APBE of pure Ni_3Al is taken as 150 J m^{-2}, in agreement with TEM observations and *ab initio* calculations [21]. Table 2 shows the values of the coefficients for the elements under consideration, including solid solution strengthening coefficients for the γ (β_i^{γ}) and γ′ phases ($\beta_i^{\gamma'}$) (refer to Section 3.3).

Table 2
APBE change and solid solution strengthening coefficients.

Coefficient	Al	Ti	Cr	Mo
k_i (mJ m^{-2}/at)	–	15	−1.7	−1.7
β_i^{γ} (MPa/at)	212	1186	375	1112
$\beta_i^{\gamma'}$ (MPa/at)	–	1830	1100	4180

3.5. Solid solution strengthening

Solid solution strengthening in the γ phase is commonly included in calculations of the overall yield strength, e.g. Ref. [8] but that in the γ′ is rarely considered, e.g. Ref. [6]. It has been shown previously that the effect of composition on the critical resolved shear stress in the γ phase of Ni alloys follows a Labusch approximation [8], where the strengthening contribution of each element (S_i^{γ}) is given as:

$$S_i^{\gamma} = \beta_i^{\gamma} x_i^{\gamma\,2/3} \tag{10}$$

Where β_i^{γ} are constants that depend on the atomic radius and modulus of element i [8].

In contrast to Equation (10), studies of the solid solution strengthening in the γ′ phase [6,22,23] have identified a linear variation with atomic concentration, with the strengthening contribution of each element in the γ′ ($S_i^{\gamma'}$) given by:

$$S_i^{\gamma'} = \beta_i^{\gamma'} x_i^{\gamma'} \tag{11}$$

Mishima et al. [22] attributed the difference in exponents to variations in atomic bonding of the alloying elements in the $L1_2$ structure, as opposed to a disordered A1 atomic arrangement, in addition to the induced local lattice and modulus distortions. Table 2 gives the values of β_i^{γ} and $\beta_i^{\gamma'}$ for the elements under consideration, obtained from the literature [22,24,25].

The total contribution from all alloying elements to the solid solution strengthening of a single phase (σ_{sss}) was determined following the approach of Gypen and Derrutere [26], by summing the individual contributions (Equations (10) and (11)) within each phase. For the γ matrix phase, this gives:

$$\sigma_{sss}\gamma = \left(1 - f_{\gamma'}\right)\left[\sum_i \left(S_i^{\gamma}\right)^{3/2}\right]^{2/3} \tag{12}$$

The compositions of the secondary and tertiary γ′ are likely to be different, giving rise to different extents of solid solution strengthening. Following the same principle as for precipitation shear in Section 3.3, the σ_{sss} of each precipitate distribution was weighted according to its relative particle number density, since the mechanisms of strengthening occur at the particle level, giving:

$$\sigma_{sss}\gamma' = f_{\gamma'}\left(\sum_i S_i^{\gamma'} \sec\frac{N_{sec}}{N_{sec}+N_{ter}} + \sum_i S_i^{\gamma'} \mathrm{ter}\frac{N_{ter}}{N_{sec}+N_{ter}}\right) \tag{13}$$

3.6. Coherency strengthening

Many models exist in the literature to describe the role of coherency strengthening [5,7,27–29], but all predict a strength increment proportional to the magnitude of the lattice misfit to the power of an exponent, typically between 1 and 1.5. In this study, the model described by Reppich [30] was used to determine the strengthening effect arising from lattice misfit (τ_{coh}), using Equation (14). This model is a compilation of existing models by other authors [4,31,32].

$$\tau_{coh} = \alpha\mu|\delta|^{3/2}\left[\frac{fr}{b}\right]^{1/2} \tag{14}$$

where δ is the experimentally determined lattice misfit, r is the average precipitate radius, and α is a constant taken as 3.7, as given in the study by Reppich [30]. Equation (14) has been defined for alloys with a monomodal size distribution of small particles and low volume fraction. In principle, the equation could be extended to account for coherency strengthening in the secondary and tertiary γ' if the lattice misfit of each distinct γ' distribution is known, similar to Equations (7) and (13). In practice, it is difficult to isolate each contribution when experimentally measuring the lattice parameters and misfit values. Since the product $(fr)^{1/2}$ is much larger for the secondary γ' than for the tertiary γ', it will be assumed in the present calculations that the radius and volume fraction in Equation (14) correspond to those of the secondary γ' as a first approximation.

3.7. Equilibrium phase composition

For comparison to experimental data, the equilibrium phase compositions of each alloy were predicted by thermodynamic modelling using the ThermoCalc software package along with the TCNi7 database. Since ThermoCalc is only able to model a single precipitate distribution, the same equilibrium composition was taken for both the secondary and tertiary γ'.

4. Experimental and modelling results

The microstructure, phase compositions and lattice parameters of each alloy were fully characterised in order to obtain the input parameters required for the models. This allowed the quantification of each strengthening mechanism and the prediction of the factors controlling the yield stress. The only material constants required for the models are the shear modulus and Burgers vector; these values were assumed equal to those for typical superalloys $\mu = 80$ GPa and b=0.248 nm [8], respectively.

Equations (6) and (14) give the shear stress increments associated with particle shear and coherency strengthening. To determine the yield stress, these shear stresses could, ideally, be converted using the Taylor factor. However, since the grain size is on the scale of mm in the present alloys, deformation is closer to that of a single crystal and compression along <001> was assumed. In the γ phase, {111}<110> slip occurs, resulting in a Schmid factor of 0.5. Therefore a multiplication factor of $m = 2$ was used to convert each shear stress to a normal stress, giving $\sigma_p = 2\tau_p$ and $\sigma_{coh} = 2\tau_{coh}$.

4.1. Particle size distribution

A characteristic STEM micrograph of each alloy is shown in Fig. 1. Each alloy contained a bimodal precipitate size distribution, comprising secondary and tertiary γ'. Secondary γ' are shown at the same magnification in the left column and the tertiary γ' are shown at the same scale in the right column. Increasing Mo content is shown vertically. The average precipitate volume fractions and sizes are shown in Table 3. Each alloy consisted of very large grains (approximately 1 grain boundary per mm) due to the VIM and homogenisation heat treatments.

It is clearly seen that the morphology of the secondary γ' changed progressively from spherical to cuboidal as the nominal Mo content of the alloy was increased. The smallest secondary γ' occurred in the 3 at.% Mo alloy (210 nm) whilst the largest occurred for the 1 at.% Mo case (463 nm). Large secondary γ' precipitates were also associated with "flowery" morphologies characteristic of splitting, as seen in a number of the alloys (Fig. 1 c, e, i and k).

In all alloys, the tertiary γ' were spherical and showed no sign of

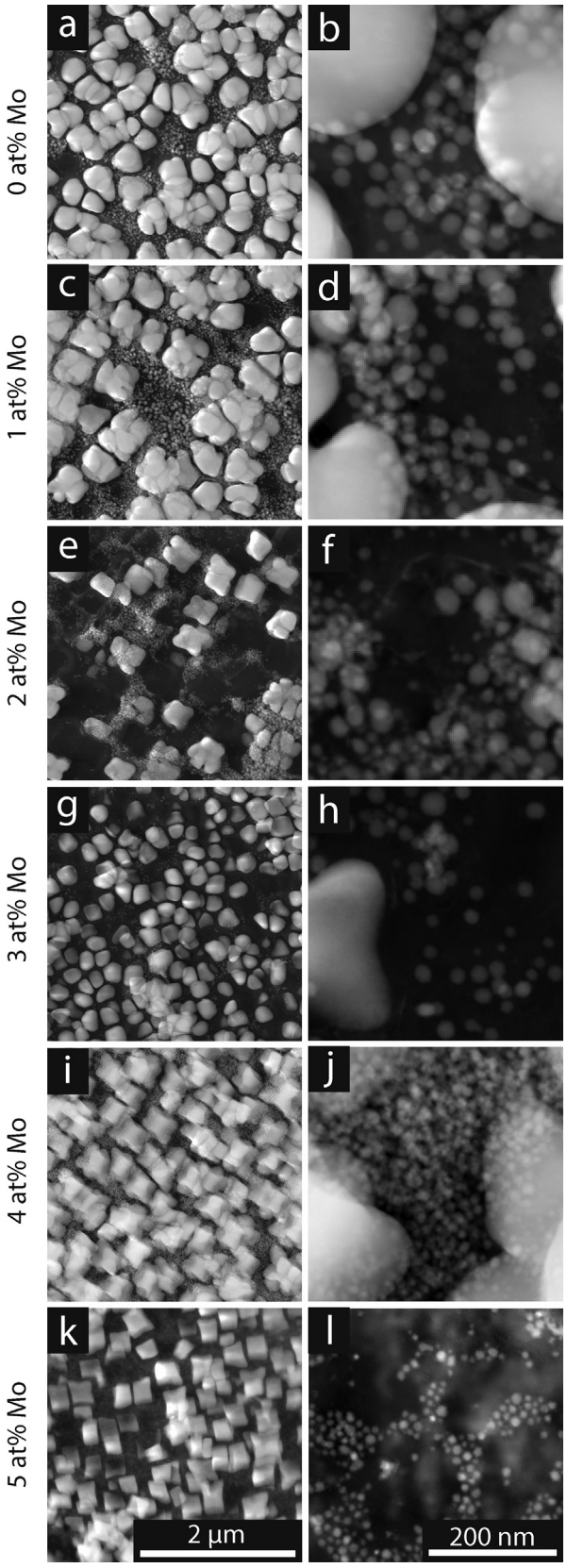

Fig. 1. STEM micrographs of extraction replicas of each alloy, containing 0 (a, b), 1 (c, d), 2 (e, f) 3 (g, h), 4 (i, j) and 5 at% Mo (k, l). Secondary γ' are displayed on the left and tertiary γ' are displayed on the right at a higher magnification.

Table 3
Experimental volume fraction of the secondary γ′ precipitates, and average size of both secondary and tertiary γ′ precipitates.

Alloy (at.%Mo)	Secondary γ′ Volume Fraction (%)	Secondary γ′ Size (nm)	Tertiary γ′ Size (nm)
0	40.3 ± 0.4	299 + 45 − 39	35 + 14 − 10
1	46.9 ± 1.0	463 + 86 − 72	36 + 20 − 13
2	39.2 ± 0.8	374 + 73 − 61	20 + 6 − 5
3	44.1 ± 0.6	210 + 38 − 32	24 + 8 − 6
4	40.0 ± 0.7	342 + 67 − 56	15 + 4 − 3
5	40.0 ± 1.0	291 + 52 − 44	13 + 5 − 4

precipitate splitting. The size of the tertiary γ′ decreased as the nominal Mo content increased. The smallest average tertiary γ′ were found in the 5 at.% Mo alloy (13 nm) whilst the largest were found in the 1 at.% Mo alloy (36 nm). The volume fraction of the tertiary γ′ is difficult to estimate with the given magnification, and was taken to be 5% for the model calculations, since the total equilibrium fraction of γ′ predicted by Thermocalc was ~45% in all alloys, and the average measured volume fraction of secondary γ′ was ~40% in most cases (Table 3).

4.2. Elemental partitioning

Large-area EDX scans showed that the composition of each of the samples was homogeneous. Average values of the experimentally measured bulk compositions are given in Table 4.

Fig. 2a, b and c show the compositions of the γ, secondary γ′ and tertiary γ′ phases respectively and how they vary across the alloy series. Solid lines represent the experimental STEM EDX data, whilst the dashed lines represent ThermoCalc predictions for the equilibrium composition of each phase. APT was carried out on the 0 at.%Mo and 3 at.%Mo samples, and these data are represented as points in Fig. 2a–c.

The experimental compositions of the γ phase showed classic elemental partitioning (Fig. 2a), with high Cr and Mo but low Al and Ti contents compared to the nominal bulk alloy composition [33]. With the exception of Mo, the composition of each element in the γ phase remained constant as the nominal Mo content of the alloy was increased from 0 to 5 at.%.

The equilibrium predictions for the composition of the γ′-partitioning elements (Al and Ti) in the γ matrix phase were very close to the experimental STEM EDX results. However, the γ-partitioning elements were less well predicted; ThermoCalc underpredicted the Cr content but overpredicted the Mo content, although the difference is small.

The secondary γ′ phase compositions also exhibited the expected elemental partitioning behaviour (Fig. 2b). The Cr and Mo contents were low, whilst the Al and Ti contents were high relative to the bulk alloy composition. As the nominal Mo content of the alloy was increased, there was a concurrent decrease in the Cr content of the secondary γ′, accompanied by a clear increase in the Mo content. The Ti content was constant throughout the alloy series and a similar argument could be made for the Al content. However, the determination of Al content by STEM EDX is prone to much more uncertainty than the other elements, due to the very low energy of the Kα emissions used to detect it. Since the emissions occur at very low energies they are easily absorbed by the sample, resulting in potentially significant underestimates of the Al content. It has been shown previously that the experimental composition of Al in the secondary and tertiary γ′ phases is significantly lower when determined by STEM EDX than by APT [10]. Therefore, the APT data was deemed to provide a more accurate value of the Al composition for the subsequent discussions.

It is seen in Fig. 2b that ThermoCalc provides reasonable predictions of the Cr and Mo content of the secondary γ′ phase, although they are slightly under- and over-predicted respectively. The over-prediction of Cr is equivalent to that in the γ phase, whereas the Mo content was under-predicted in the γ. The equilibrium predictions of the Ti content in the secondary γ′ were very far above those measured experimentally. However, the Al content, as measured by APT, was relatively consistent with the ThermoCalc predictions.

Fig. 2c shows the experimentally determined composition of the tertiary γ′ across the alloy series, along with the predicted equilibrium composition. High concentrations of Al and Ti exist in the tertiary γ′ phase, as expected from classical partitioning theory. In comparison with the secondary γ′, the tertiary γ′ have higher Al contents and lower Ti contents. Notably, unexpectedly high contents of the γ-partitioning elements (Cr and Mo) were measured in the tertiary γ′ phase, compared to the nominal bulk alloy composition. This was not predicted by ThermoCalc.

Overall, there was more variation within the experimental compositions of the tertiary γ′ phase, and there was a weaker correlation with the equilibrium ThermoCalc predictions than seen with the γ phase and secondary γ′. The equilibrium Cr content was predicted by ThermoCalc to decrease as the nominal Mo content of the alloy increased, contraposing the experimental data. The equilibrium prediction of the Mo content of the tertiary γ′ was negligible, in stark contrast to the experimental data. For example, ThermoCalc predicted the Mo content of the tertiary γ′ to be 0.13 at.% in the nominally 5 at.%Mo alloy, which differed markedly from the experimentally determined concentration of 3.6 ± 0.9 at.%.

Table 4
The bulk composition of each alloy, as determined experimentally by STEM EDX.

Alloy (at.%Mo)	Mean Composition (at.%)				
	Al	Ti	Cr	Mo	Ni
0	5.9 ± 0.5	5.09 ± 0.06	15.2 ± 0.1	0	73.8 ± 0.2
1	6.1 ± 0.4	5.0 ± 0.1	15.4 ± 0.3	0.69 ± 0.05	72.9 ± 0.4
2	6.0 ± 0.2	5.22 ± 0.09	15.4 ± 0.1	1.72 ± 0.08	71.7 ± 0.2
3	5.7 ± 0.1	5.1 ± 0.1	15.2 ± 0.2	2.66 ± 0.06	71.4 ± 0.2
4	5.5 ± 0.3	5.12 ± 0.02	15.4 ± 0.1	3.55 ± 0.06	70.5 ± 0.2
5	5.7 ± 0.2	5.1 ± 0.1	15.5 ± 0.4	4.5 ± 0.2	69.3 ± 0.3

4.3. Solid solution strengthening

Fig. 2d–f illustrate the predicted effect that the phase compositions have on solid solution strengthening in each phase across the alloy series. The increasing Mo content causes an increase in strength of the γ phase by almost 200 MPa (Fig. 2d), principally associated with the increase of ~7 at.% Mo in the γ matrix phase. The high Mo content in the tertiary γ′ also has a significant effect on the solid solution strengthening of this phase (Fig. 2f), with the ~4 at.% Mo giving rise to ~150 MPa of strengthening to the tertiary γ′. Within the γ matrix phase, Cr is also seen to have a significant effect on the solid solution strengthening, due to its high

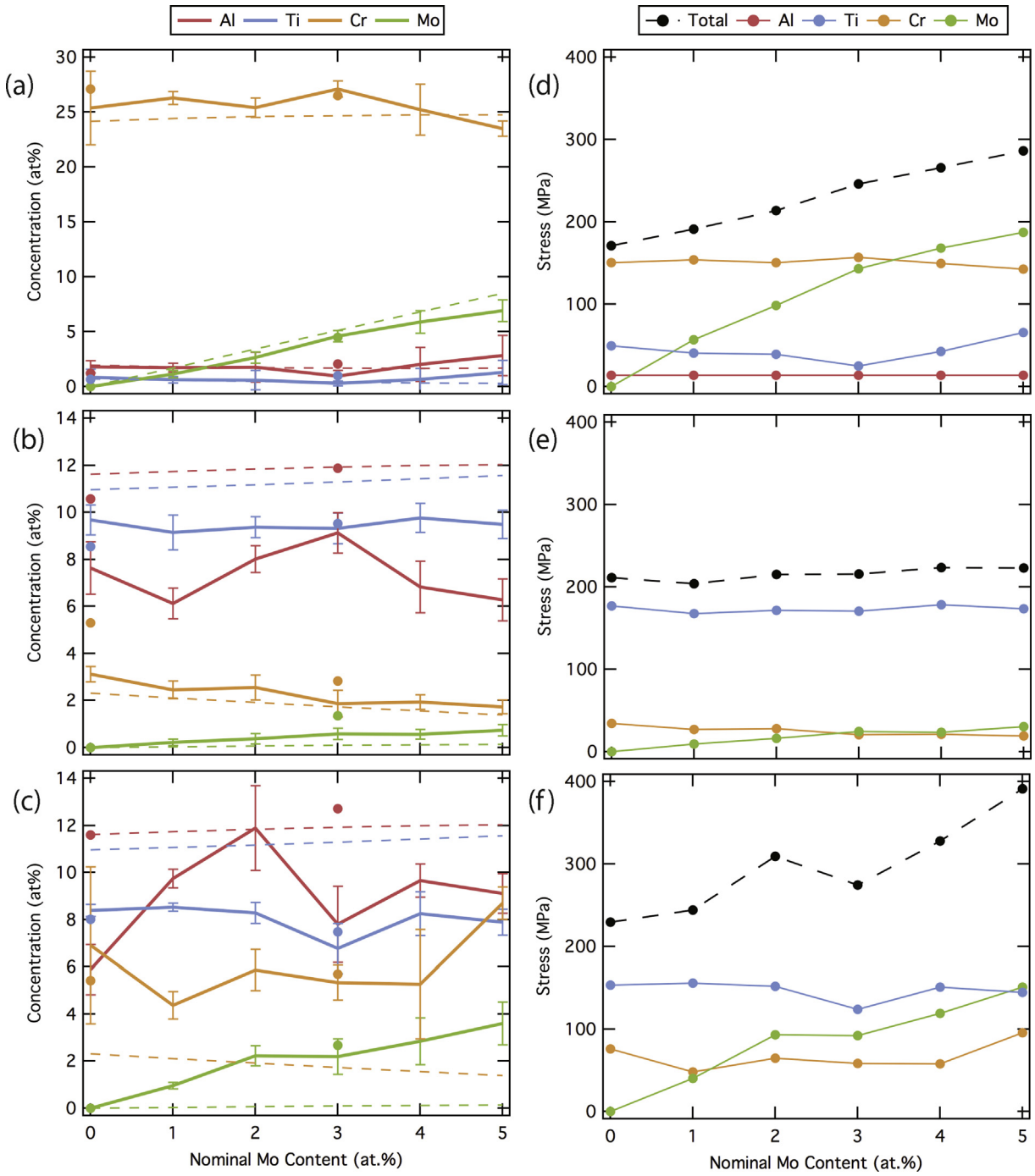

Fig. 2. Composition of the γ phase (a), the secondary γ′ phase (b) and the tertiary γ′ phase (c), as a function of the nominal Mo content. Solid lines represent experimental STEM EDX data, points represent experimental APT data, and ThermoCalc equilibrium composition predictions using the TCNi7 database are shown as dashed lines. The ensuing effect on the extent of solid solution strengthening in the γ (d), secondary γ′ (e) and tertiary γ′ (f) is given on the right.

concentration within that phase. In contrast, in the γ′ precipitate phases, the main contribution to solid solution strengthening comes from the Ti.

The tertiary γ′ phase benefited from greater solid solution strengthening than either the γ or secondary γ′ phases. Mo has the strongest effect on the tertiary γ′ (Fig. 2f), increasing the solid solution strength from 220 MPa (in the 0Mo alloy) to 400 MPa (in the 5Mo alloy). This significant increase in strength would not have been obtained if it were assumed that the tertiary γ′ had the equilibrium compositions predicted by ThermoCalc.

4.4. Lattice misfit and coherency strengthening

The lattice parameters of the γ and γ′ phases, and the associated lattice misfits are shown as a function of nominal Mo content in Fig. 3. For comparison to experimental data, a value for the *predicted* lattice parameter (a) of each phase at 760 °C was attained using Equation (15). Predictions of the molar volumes (V_m) of each phase were made with ThermoCalc, using both the experimentally determined phase compositions, and the predicted equilibrium compositions. Subsequent calculation of the lattice misfit (δ) was

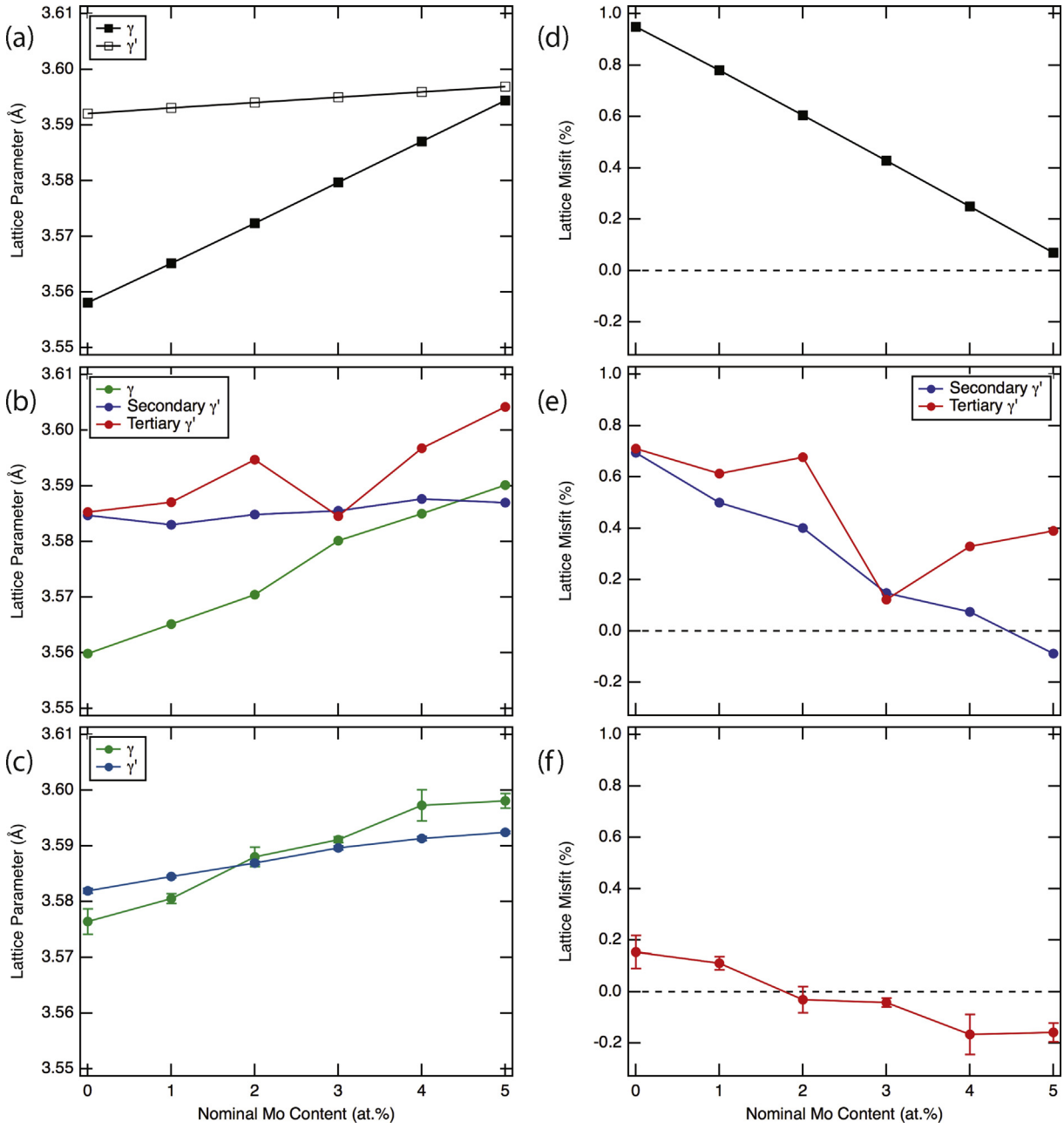

Fig. 3. Lattice parameters (a) and lattice misfit (d) predicted by ThermoCalc using the equilibrium phase compositions with the TCNi7 database. Lattice parameters (b) and lattice misfit (e) predicted by ThermoCalc using the experimental phase compositions with the TCNi7 database. Experimental lattice parameters (c) and lattice misfit (f) determined by neutron diffraction. All given as function of the nominal alloy Mo content.

via Equation (4).

$$a = \left(\frac{4V_m}{N_A}\right)^{1/3} \tag{15}$$

Where (N_A) is the Avogadro constant. Fig. 3a and d show the lattice parameters and lattice misfit, respectively, predicted by ThermoCalc using the equilibrium predicted phase compositions. It should be noted that ThermoCalc only predicts one composition for the γ′ phase, the equilibrium value. Fig. 3b and e display the lattice parameters and lattice misfit of the alloys predicted by ThermoCalc using the experimental phase compositions found via STEM EDX and APT. The differing phase compositions of the secondary and tertiary γ′ result in differing lattice parameters and misfit. Finally, Fig. 3c and f show the experimental lattice parameters and misfit determined by neutron diffraction. Due to the low volume fraction of the tertiary γ′, the diffraction data associated with this population could not be separated from that of the secondary γ′, which dominated the diffraction data. As such, the lattice parameters quoted are those of the γ and secondary γ′ phases only.

The ThermoCalc predictions of the γ and γ′ phase compositions at equilibrium resulted in linear increases in the matrix and precipitate phase lattice parameters with nominal Mo content (Fig. 3a). This, in turn, resulted in a linear decrease in the predicted lattice misfit with increasing Mo content (Fig. 3d), since the lattice parameter of the matrix phase increased faster than that of the precipitate phase.

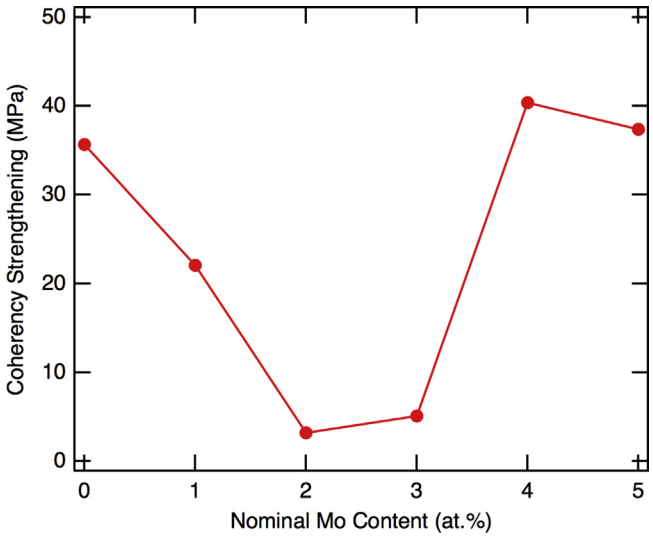

Fig. 4. Extent of coherency strengthening from the experimentally measured lattice parameters, as a function of nominal alloy Mo content.

When ThermoCalc was used to predict the lattice parameters and misfit resulting from the experimental phase compositions, the general trends with Mo content were the same as those using equilibrium compositions. However, the magnitudes differed and the trends were significantly less linear (Fig. 3b and e). Experimentally, the secondary and tertiary γ′ precipitates have different compositions, resulting in a greater lattice parameter in the tertiary γ′ phase. In turn, this produces a larger lattice misfit between the γ matrix and the tertiary γ′ phase. The lattice parameter of the secondary γ′ phase was approximately constant, at ~3.585 Å, across the alloy series investigated. The 5 at.% Mo alloy alone was predicted to have a negative lattice misfit between the γ matrix and the secondary γ′ phase.

The experimental lattice parameters of the matrix and precipitate phases measured were found to increase with the nominal alloy Mo content (Fig. 3c and f), as predicted by ThermoCalc. However, the experimental diffraction data indicated that the two phases had much more similar lattice parameters than those predicted using the ThermoCalc-based method. Although, it must be noted that neutron diffraction measured the constrained lattice parameters, whereas ThermoCalc predicted the unconstrained values. The experimentally measured lattice misfit was seen to decrease as nominal Mo content was increased, becoming negative between 1 and 2 at.% Mo. However, the magnitude of the lattice misfit of the 0 and 5 at.% Mo alloys were approximately the same, at ~0.15%.

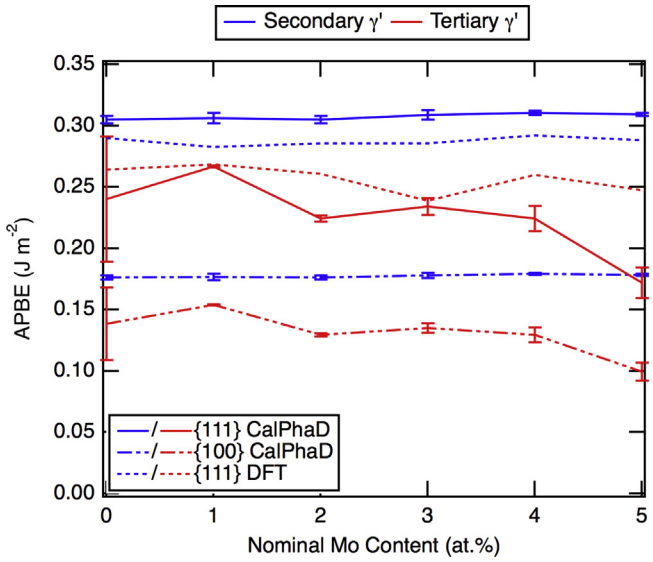

Fig. 5. Predicted APBE for the secondary and tertiary γ′ as a function of nominal alloy Mo content. Predictions from a CalPhad approach are given as solid lines for the {111} planes, and dashed/dotted lines for the {100} planes. Predictions from a DFT approach are given as dotted lines.

The changing Mo content across the alloy series resulted in a decreasing lattice misfit, which influences the yield strength through coherency strengthening. The effect of the experimentally determined lattice misfit on the overall yield strength is shown in Fig. 4. As seen in Equation (14), the coherency strengthening increment is anticipated to be proportional to the magnitude of the lattice misfit to the power of 3/2. Hence, the predicted coherency strength increment, (Fig. 4), is largest for the low and high Mo content alloys, where the lattice misfit has the largest magnitude (Fig. 3). Similarly, the very low lattice misfits of the alloys with 2 and 3 at.% Mo result in negligible coherency strengthening. The maximum coherency strengthening contribution was predicted to be only ~40 MPa in the alloys studied.

4.5. Anti-phase boundary energy and precipitation shear

The Anti-Phase Boundary Energies (APBEs) that were obtained using the experimental phase compositions of the alloys are shown in Fig. 5. Using both the CalPhaD and DFT approaches for relating the experimental γ′ compositions to the APBE, the APBE of the secondary γ′ was determined to remain approximately constant as the nominal Mo content of the alloy was increased, although the two approaches yielded slightly different values. With CalPhaD, an APBE of ~310 mJ m^{-2} was obtained for the secondary γ′ on {111}, compared to ~290 mJ m^{-2} using DFT.

The APBE of the tertiary γ′ was calculated to be lower than that of the secondary γ′. Using the CalPhaD approach, the APBE decreased from 240 ± 5 mJ m^{-2} to 172 ± 1 mJ m^{-2} on the {111} planes as the nominal bulk Mo content was increased from 0 to 5 at.%, whereas with the DFT approach it was calculated to decrease from ~260 mJ m^{-2} to ~250 mJ m^{-2}. These variations correspond to an experimental Mo increase in the secondary γ′ of 0–3.6 ± 0.9 at.% Mo. For both precipitate distributions, the APBE on {100} was ~125 mJ m^{-2} lower than that on the {111}. Although the trends in APBE values using both approximations were in agreement, the CalPhaD approach suggested greater effects from variations in Mo and Cr.

The effect of the APBE on the overall alloy yield strength arising from precipitate hardening is shown in Fig. 6, in which calculations for APBE by both CalPhaD and DFT methods are shown. The extent of precipitation strengthening from the secondary γ′ phase was predicted to be almost exactly the same by both methods (and therefore indistinguishable in Fig. 6), since the predicted APBEs were very similar. However, CalPhaD and DFT approximations of the APBE gave different results for the extent of precipitation strengthening by the tertiary γ′ phase. The trend with nominal alloy Mo content was less pronounced using the DFT method. It is worth noting that the extent of precipitation strengthening by the tertiary γ′ in these alloys is an order of magnitude greater than that of the secondary γ′, even though the volume fraction is only 5%, compared to ~40% for the secondary γ′.

4.6. Yield stress: experiments vs. modelling

The effect of nominal Mo content on the experimental

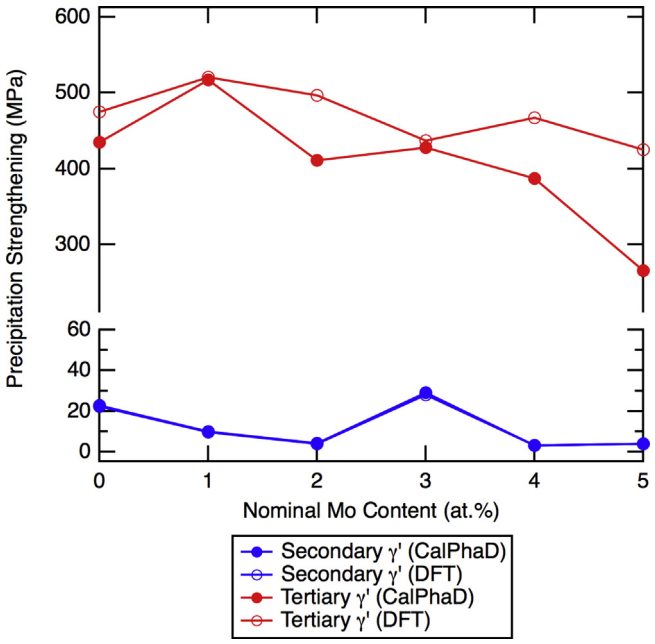

Fig. 6. Extent of precipitation strengthening arising from the secondary and tertiary γ′ precipitates as a function of nominal alloy Mo content. Predictions using the CalPhaD approach are given as closed circles, whilst DFT predictions are given as open circles.

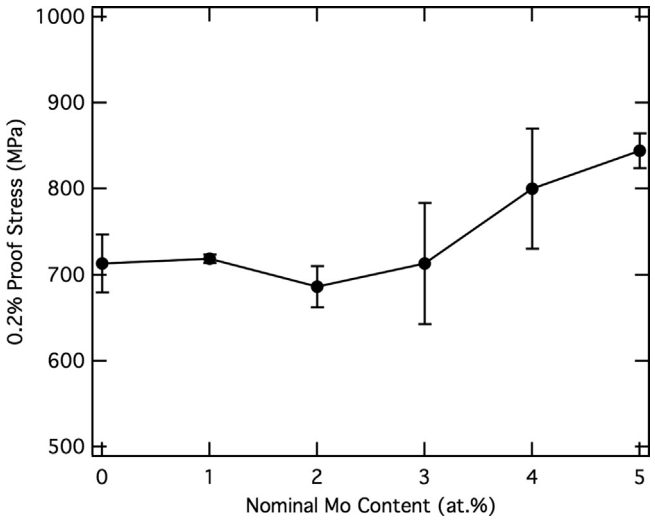

Fig. 7. Experimental 0.2% proof stress at room temperature as a function of the nominal Mo content of the alloy.

compressive strength of the alloys with varying Mo content is shown in Fig. 7. Increasing the nominal Mo content from 0 to 5 at.% raised the 0.2% compressive proof stress from 710 ± 30 MPa to 840 ± 20 MPa.

The overall modelled yield strength as a function of nominal Mo content is shown in Fig. 8, in addition to a breakdown of the contributions from the individual strengthening mechanisms. The experimental room temperature compressive strength is also shown for comparison. Fig. 8a gives the model predictions obtained using the CalPhaD approach for the APBE calculation, whereas Fig. 8b uses the DFT approach. When the CalPhaD method was used to calculate the APBE, the overall yield strength followed the experimental fluctuations well up to 3 at.% Mo. However, with higher Mo additions it decreased to a minimum value of ~680 MPa.

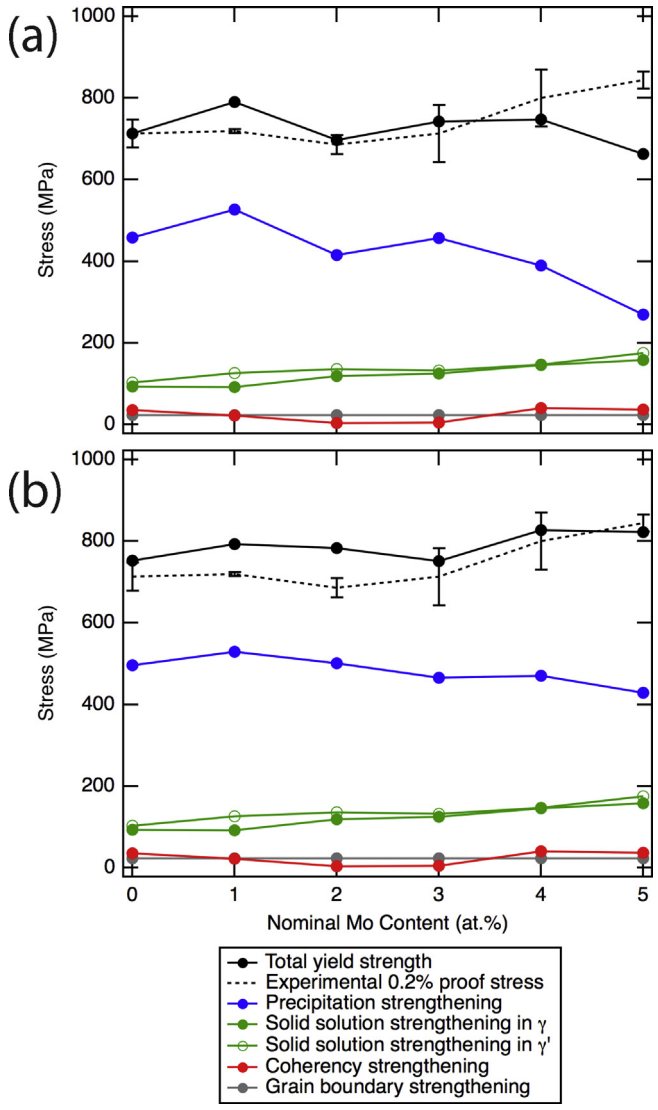

Fig. 8. Contributions to the total yield strength as a function of nominal alloy Mo content, using a CalPhaD approach (a) and a DFT approach (b) for the calculation of precipitation strengthening.

This is in contrast to the increasing experimental compressive strength. When the DFT approach was used to determine the APBE, there was a less marked decrease in the extent of precipitation strengthening across the alloy series, and the predicted yield strength was more consistent with the experimental trend, particularly at higher Mo contents. This suggests that the influence of Mo and Cr on the APBE is not as pronounced as it is predicted using the CalPhaD approach.

The extent of solid solution strengthening in the γ matrix phase increases with nominal Mo content. Notably, so does that of the γ′ precipitate phase. The contribution of coherency strengthening does not vary linearly (Fig. 4), and is very low. Similarly, the role of grain boundary strengthening in the alloy series studied is negligible, due to the very large grain size present in the microstructures.

5. Discussion

Comparison of the experimental and modelled phase compositions indicate that ThermoCalc was capable of accurately

predicting the composition of the γ matrix phase, and suitably predicted the content of the γ-partitioning elements of the secondary γ′ phase. However, it could not be used as a tool for reliable prediction of the Ti content of the precipitate phases, and most clearly, was unable to predict the composition of the tertiary γ′. This limitation is to be expected as the tertiary precipitates form from the supersaturated solid solution at lower temperatures during cooling and, as such, there is limited opportunity for solute exchange to occur via diffusion between the phases present [34]. This results in a composition of the secondary γ′ that is closer to the expected values for equilibrium. However, it should be noted that the non-equilibrium compositions of the tertiary γ′ may be retained during high temperature exposure for many hundreds of hours [10].

Increasing the bulk Mo content was seen to have little to no effect on the partitioning of the Al, Ti or Cr within the matrix phase (Fig. 2a). The same can be said for the Ti content of the secondary and tertiary γ′ precipitates (Fig. 2b and c). However, it is clear that the increasing bulk Mo content across the alloy series did have an effect on the partitioning of Cr in the secondary γ′, with a higher Mo content. However, it is difficult to ascribe a trend to the Cr content in the tertiary γ′ due to larger scatter in the experimental data.

The composition of each phase directly affects the extent of solid solution strengthening. Table 2 shows that Mo is the most potent solid solution strengthener in the γ′ precipitate phase [22] and that Ti and Mo additions have the largest effect on solid solution strengthening in the γ matrix phase [8]. These effects are evident in Fig. 2d–f. It can be seen that the Ti content actually had the largest contribution to solid solution strengthening in the secondary γ′ phase, since the contents of other potent strengtheners in this phase were very low. In contrast, although it is the most potent solid solution strengthener in the γ phase, Ti had very little effect due to its low concentration in the matrix. Instead, Cr provided the most significant strengthening contribution. As expected, in the γ matrix, the solid solution strengthening of Mo increased with its nominal content in the alloy, becoming the most potent strengthener in the 4 and 5 at.% Mo alloys. A very similar trend was visible in the tertiary γ′ phase. The magnitude of the total solid solution strengthening in the γ and tertiary γ′ phases increased with nominal Mo content across the alloy series, although the contribution of the secondary γ′ was approximately constant.

The largest strengthening effect is shown to arise through precipitation strengthening, for which the presence of Mo in these alloys is significant. Mo is classically expected to partition to the matrix phase and therefore have a minimal effect on the APBE of the γ′. In this study it is shown that the tertiary γ′ phase had a substantial Mo content, with a resulting decrease in the APBE. Consequently, there was a decrease in the predicted precipitation strengthening in these alloys (Figs. 6 and 8). This was more significant when using the CALPHAD method for APBE determination, than when using the DFT approach. Importantly, the extent of precipitation strengthening from the tertiary γ′ was an order of magnitude larger than that from the secondary γ′ (Fig. 6). This is due to the size of the former being closer to the optimum for precipitate shearing resistance, in addition to the fact that there is a larger number density of tertiary γ′. Therefore, the secondary γ′ precipitates offer less resistance to dislocation motion, and provide a smaller contribution to the overall alloy strength.

The APBEs shown in Fig. 5 were calculated using the experimental phase compositions of each alloy, in which the content of each element varies (except Al). To determine the effect of the Mo content alone, the APBE was again estimated with the experimental Mo content, but with an average constant value for the content of the Al, Ti and Cr (not shown). This also resulted in a decreasing APBE as the nominal (and experimental) Mo content was increased. It is therefore clear that Mo additions have the effect of reducing the APBE in these alloys. This has been shown previously [21] using both the CalPhaD and DFT methods. The former approach suggested that Mo additions up to 5 at.% increased the APBE, which subsequently decreased upon further Mo additions. Using the DFT approach, the APBE was predicted to decrease from the outset with Mo additions. Both of these results are consistent with the present work.

Using the CalPhaD method to calculate the APBE from the experimental phase compositions resulted in a slight decrease in the predicted yield strength. This is in contrast to the experimentally measured yield strength (Fig. 7), which displayed a clear rise as the nominal Mo content was increased. On the contrary, using the DFT approach to calculate the APBE resulted in an overall yield strength which followed the same trend as that seen experimentally – increasing with nominal alloy Mo content. In either case, the extent of precipitation strengthening was clearly shown to decrease as nominal alloy Mo content increased.

In terms of coherency strengthening, the smallest strengthening contribution was seen for the 2 and 3 at.% Mo alloys (Fig. 4), in which the magnitude of the experimentally measured lattice misfit was a minimum (Fig. 3). The magnitude of the experimentally measured lattice misfit, and therefore the coherency strengthening, was similar for the 0 and 5 at.% Mo alloys, although the low Mo alloys displayed a positive misfit and the high Mo alloys showed a negative misfit. This gives rise to a non-linear coherency strengthening effect across the alloy series. The trends in the lattice misfit between the γ matrix and the secondary γ′ predicted using ThermoCalc and the experimentally measured phase compositions (Fig. 3e) were in better agreement with experiment (Fig. 3f) than those of the tertiary γ′. This confirmed that the misfit decreased with increasing Mo content of the alloy. The predicted misfit in the tertiary γ′ also decreased up to 3 at.% Mo, although it increased again for the 3 at.% Mo and 4 at.% Mo alloys. This could be attributed to the higher Mo content within the tertiary γ′ phase in these alloys. These results indicate that the assumption of modelling the coherency strengthening arising from only the secondary γ′ precipitates (Equation (14)) gives consistent results to the experimental variations of the total lattice misfit. The contribution to the yield stress from coherency strengthening was predicted to be significantly smaller than other contributions. Therefore, it cannot account for the differences in the trends between the predicted and experimental yield stresses.

The increasing yield stress cannot be attributed to differences in the volume fraction of the γ′ precipitates as there was no significant trend in the volume fraction of secondary γ′ with nominal alloy Mo content, which was approximately constant around 40%. The only contribution to strength that increased across the alloy series was that of solid solution strengthening. In this regard, it should be noted that the solid solution strengthening of the ordered γ′ precipitate phase is as significant as that of the matrix phase. This result is not prevalent in the literature. Without the solid solution strengthening effect of the γ′ precipitate phase, the yield strength predictions would be significantly divergent from the experimental results. The increased strength (~150 MPa in the nominally 5 at.% Mo alloy) can therefore be attributed to the significantly increased solid solution strengthening caused by the presence of Mo in the tertiary γ′ precipitate phase. To the authors' knowledge, this is the first time that such effects have been reported and predicted in superalloys with varying Mo additions.

To demonstrate the significance of this effect, Fig. 9 was plotted showing model predictions for each strengthening component, using the equilibrium phase compositions determined by ThermoCalc. The DFT method was used to calculate the APBE from the equilibrium phase composition, and therefore the extent of

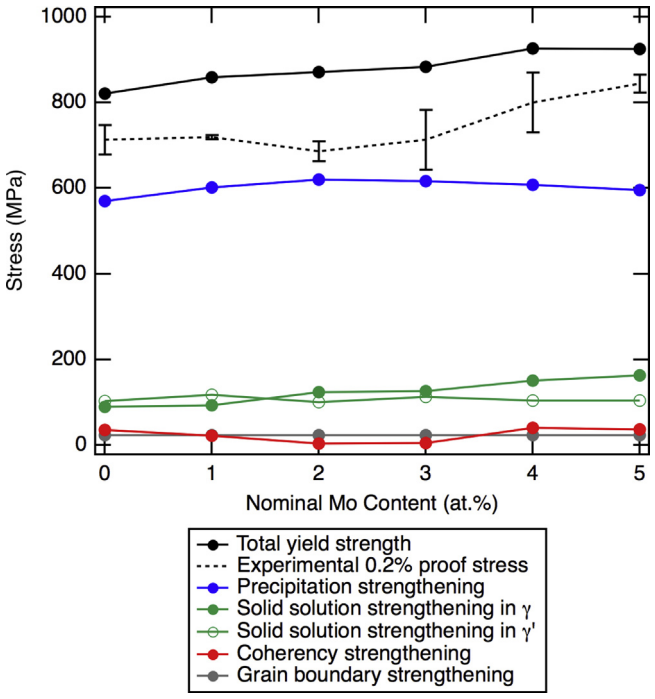

Fig. 9. Contributions to total yield strength using a DFT approach to precipitation strength calculation, when the equilibrium phase compositions predicted by ThermoCalc and the TCNi7 database are used.

precipitation strengthening. All other factors, such as precipitate size and volume fraction, were consistent with the previous data (Fig. 8). It is clearly evident that by approximating phase compositions to those at equilibrium (ThermoCalc), the experimental yield strength cannot be reproduced. Notably, the contribution from precipitation strengthening is much greater using the predicted equilibrium compositions than those determined experimentally. This disparity is most marked for the alloys containing the highest Mo concentrations, where the extent of precipitation strengthening differs by ~200 MPa. In addition, the contribution from solid solution strengthening of the γ′ precipitate phase is lower with calculations based on the predicted equilibrium phase composition, which remained constant across the alloy series. Since the equilibrium predictions for the composition of the γ phase were similar to those found experimentally, the extent of solid solution strengthening in the matrix phase is consistent using both experimental and modelled compositions.

Overall, approximating phase compositions to those predicted at equilibrium resulted in much higher yield strengths for all alloys studied, and these are not representative of the actual alloy behaviour. The yield strength is well predicted using the experimental phase composition data, due to the solid solution strengthening of the ordered γ′ precipitate phase, and the decreasing degree of precipitation strengthening as the Mo content of the γ′ phase is increased.

6. Conclusion

The yield strength of a model polycrystalline Ni-based superalloy with varying Mo content has been predicted using current models available in the literature. Using a CalPhaD approach for calculating the APBE from the experimentally measured phase compositions, the alloy strength was predicted to remain approximately constant with nominal Mo content, with some evidence of a decrease for alloys with the highest Mo concentrations. This is in contradiction to the experimental strength increase measured by compression testing. This disparity is principally attributed to the decreasing magnitude of the APBE in the tertiary γ′ phase with addition of Mo. In contrast, using a linear DFT approach to the APBE calculations from the experimentally measured phase compositions, there was good agreement with the experimental results. Of all the hardening mechanisms present, that of precipitation strengthening resulted in the largest contribution to alloy strength. The effect of solid solution strengthening in the γ matrix phase was significant, giving up to ~300 MPa additional strength. However, notably, the solid solution strengthening effect of the ordered γ′ phase was also substantial, and equivalent to that of the matrix phase. Evidently, the effect of solid solution strengthening in the ordered phase must be taken into account when modelling the mechanical properties of Ni-based superalloys. Without this strengthening mechanism, the yield strength of Ni-based superalloys cannot be accurately predicted.

Acknowledgements

The authors wish to acknowledge Mrs. S. Rhodes, Dr. H. T. Pang, Dr. D. M. Collins, and Dr. O. M. D. M. Messé for their assistance with the experiments performed. Funding was provided by the EPSRC/Rolls-Royce Strategic Partnership under EP/M005607/1 and EP/H022309/1. The Oxford Atom Probe facility was funded by the EPSRC under EP/M022803/1. E. I. Galindo-Nava would like to acknowledge the Royal Academy of Engineering for his fellowship funding. Neutron diffraction beam time was supported through the Canadian Neutron Beam Centre under Experiment number 1258. The original research data is available at https://doi.org/10.17863/CAM.22795.

References

[1] R.C. Reed, The Superalloys, first ed., Cambridge University Press, Cambridge, 2006.
[2] A.J. Ardell, Precipitation hardening, Metall. Trans. A 16 (1985) 2131–2165.
[3] B. Reppich, Some new aspects concerning particle hardening mechanisms in γ′ precipitating Ni-base alloys, Acta Metall. 30 (1982) 87–94.
[4] V. Gerold, H. Haberkorn, On the critical resolved shear stress of solid solutions containing coherent precipitates, Phys. Status Solidi 16 (1966) 675–684.
[5] T.A. Parthasarathy, S.I. Rao, D.M. Dimiduk, A fast spreadsheet model for the yield strength of superalloys, Superalloys, TMS (2004) 887–896.
[6] R.W. Kozar, A. Suzuki, W.W. Milligan, J.J. Schirra, M.F. Savage, T.M. Pollock, Strengthening mechanisms in polycrystalline multimodal nickel-base superalloys, Metall. Mater. Trans. 40 (2009) 1588–1603.
[7] D.A. Grose, G.S. Ansell, The influence of coherency strain on the elevated temperature tensile behavior of Ni-15Cr-Al-Ti-Mo alloys, Metall. Trans. A 12 (1981) 1631–1645.
[8] E.I. Galindo-Nava, L.D. Connor, C.M.F. Rae, On the prediction of the yield stress of unimodal and multimodal γ′ nickel-base superalloys, Acta Mater. 98 (2015) 377–390.
[9] M.R. Ahmadi, E. Povoden-Karadeniz, L. Whitmore, M. Stockinger, A. Falahati, E. Kozeschnik, Yield strength prediction in Ni-base alloy 718Plus based on thermo-kinetic precipitation simulation, Mater. Sci. Eng. 608 (2014) 114–122.
[10] A.J. Goodfellow, E.I. Galindo-Nava, K.A. Christofidou, N.G. Jones, P.A.J. Bagot, C.D. Boyer, M.C. Hardy, H.J. Stone, Gamma prime precipitate evolution during aging of a model nickel-based superalloy, Metall. Mater. Trans. 49 (3) (March 2018) 718–728. https://doi.org/10.1007/s11661-017-4336-y.
[11] J.Y. Hwang, S. Nag, A.R.P. Singh, R. Srinivasan, J. Tiley, H.L. Fraser, R. Banerjee, Evolution of the γ/γ′ interface width in a commercial nickel base superalloy studied by three-dimensional atom probe tomography, Scripta Mater. 61 (2009) 92–95.
[12] P.A.J. Bagot, O.B.W. Silk, J.O. Douglas, S. Pedrazzini, D.J. Crudden, T.L. Martin, M.C. Hardy, M.P. Moody, R.C. Reed, An Atom Probe Tomography study of site preference and partitioning in a nickel-based superalloy, Acta Mater. 125 (2017) 156–165.
[13] C.A. Schneider, W.S. Rasband, K.W. Eliceiri, NIH image to ImageJ: 25 years of image analysis, Br. J. Pharmacol. 9 (2012) 671–675.
[14] D. Freedman, P. Diaconis, On the histogram as a density estimator: L_2 theory, Z. Wahrscheinlichkeitstheor. Verwandte Geb. 57 (1981) 453–476.
[15] J.B. Nelson, D.P. Riley, An experimental investigation of extrapolation methods in the derivation of accurate unit-cell dimensions of crystals, Proc. Phys. Soc. Lond. 57 (1945) 160–177.

[16] H.J. Stone, T.M. Holden, R.C. Reed, On the generation of microstrains during the plastic deformation of waspalloy, Acta Mater. 47 (1999) 4435–4448.
[17] D.M. Collins, L. Yan, E.A. Marquis, L.D. Connor, J.J. Ciardiello, A.D. Evans, H.J. Stone, Lattice misfit during ageing of a polycrystalline nickel-base superalloy, Acta Mater. 61 (2013) 7791–7804.
[18] A.J.E. Foreman, M.J. Makin, Dislocation movement through random arrays of obstacles, Phil. Mag. 14 (1966) 911–924.
[19] T.J. Koppenaal, D. Kuhlmann-Wilsdorf, The effect of prestressing on the strength of neutron-irradiated copper single crystals, Appl. Phys. Lett. 4 (1964) 59–61.
[20] J. Friedel (Ed.), Dislocations, Addison-Wesley, Reading, 1964.
[21] D.J. Crudden, A. Mottura, N. Warnken, B. Raeisinia, R.C. Reed, Modelling of the influence of alloy composition on flow stress in high-strength nickel-based superalloys, Acta Mater. 75 (2014) 356–370.
[22] Y. Mishima, S. Ochiai, M. Yodogawa, T. Suzuki, Mechanical properties of Ni_3Al with ternary addition of transition metal elements, Trans. Of the Japan Institute of Metals 27 (1986) 41–50.
[23] J.A. Lopez, G.F. Hancock, The effects of non-stoichiometry and titanium additions on the mechanical behaviour of Ni_3Al (γ'), Phys. Status Solidi 2 (1970) 469–474.
[24] Y. Mishima, S. Ochiai, N. Hamao, M. Yodogawa, T. Suzuki, Solid solution hardening of nickel – role of transition metal and B-subgroup solutes, Trans. Of the Japan Institute of Metals 27 (1986) 656–664.
[25] M.C. Maguire, G.R. Edwards, S.A. David, Weldability and hot ductility of chromium-modified Ni_3Al alloys, Welding research (1992) 231–242.
[26] L.A. Gypen, A. Deruyttere, Multi-component solid solution hardening, J. Mater. Sci. 12 (1977) 1028–1033.
[27] S.M. Pickard, S. Schmauder, D.B. Zahl, A.G. Evans, Effects of misfit strain and reverse loading on the flow strength of particulate-reinforced A1 matrix composites, Acta Metall. Mater. 40 (1992) 3113–3119.
[28] E.J. Lee, A.J. Ardell, Superposition of precipitation-hardening mechanisms, Strength of Metals and Alloys 1 (1979) 633–638.
[29] J.M. Oblak, D.F. Paulonis, D.S. Duvall, Coherency strengthening in Ni base alloys hardened by DO_{22} γ'' precipitates, Metall. Trans. 5 (1974) 143–153.
[30] B. Reppich, Particle strengthening, in: R.W. Cahn, P. Haasen, E.J. Kramer (Eds.), Plastic Deformation and Fracture of Materials, Materials Science and Technology, vol. 6, Cambridge, Weinheim, New York, Basel, 1993, pp. 311–357.
[31] L.M. Brown, R.K. Ham, Strengthening methods in crystals, in: A. Kelly, R.B. Nicholson (Eds.), Elsevier Publishing Company, London, 1971, pp. 9–37.
[32] B. Jansson, A. Melander, On the critical resolved shear stress from misfitting particles, Scripta Metall. 12 (1978) 497–498.
[33] A.K. Jena, M.C. Chaturvedi, The role of alloying elements in the design of nickel-base superalloys, J. Mater. Sci. 19 (1984) 3121–3139.
[34] R. Radis, M. Schaffer, M. Albu, G. Kothleitner, P. Pölt, E. Kozeschnik, Multimodal size distributions of γ' precipitates during continuous cooling of UDIMET 720 Li, Acta Mater. 57 (2009) 5739–5747.